# High rate performance for carbon-coated Na3V2(PO4)2F3 in Na-Ion Batteries

Thibault Broux, François Fauth, Nikita Hall, Yohann Chatillon, Matteo Bianchini, Tahya Bamine, Jean-Bernard Leriche, Emmanuelle Suard, Dany Carlier, Yvan F. Reynier, et al.

HAL Id: hal-02103530

https://hal.science/hal-02103530

Submitted on 1 Oct 2020

# High Rate Performance for Carbon Coated Na3V2(PO4)2F3 in Na-ion batteries

*Thibault. Broux* [1,2,6,7], *François Fauth* [3], *Nikita Hall* [4], *Yohann Chatillon* [4], *Matteo Bianchini* [1,2,5], *Tahya Bamine* [1,6], *Jean-Bernard Leriche* [2], *Emmanuelle Suard* [5], *Dany Carlier* [1,6], *Yvan Reynier* [4], *Loïc Simonin* [4], *Christian Masquelier* [2,6,7] *and Laurence Croguennec* [1,6,7,] *

1 CNRS, Univ. Bordeaux, Bordeaux INP, ICMCB UMR 5026, F-33600 Pessac, France.
[2] Laboratoire de Réactivité et de Chimie des Solides, CNRS-UMR#7314,
Université de Picardie Jules Verne, F-80039 Amiens Cedex 1, France
[3] CELLS - ALBA synchrotron, E-08290 Cerdanyola del Vallès, Barcelona, Spain
[4] Univ. Grenoble Alpes, F-38000 Grenoble,
CEA, LITEN, 17 rue des Martyrs, F-38054 Grenoble cedex 9, France
[5] Institut Laue-Langevin, 71 Avenue des Martyrs, F-38000 Grenoble, France
[6] RS2E, Réseau Français sur le Stockage Electrochimique de l'Energie,
FR CNRS 3459, F-80039 Amiens Cedex 1, France
[7] ALISTORE-ERI European Research Institute, FR CNRS 3104, F-80039 Amiens Cedex 1,
France

*Corresponding author (L. Croguennec): Laurence.Croguennec@icmcb.cnrs.fr

**Abstract**

The electrochemical and structural properties of a series of three different $Na_3V_2(PO_4)_2F_3$ samples (with or without carbon coatings of different natures) obtained via different synthesis methods are compared through operando high resolution synchrotron X-Ray diffraction. The pristine materials all possess negligible quantities of oxygen defects, as probed by the b/a lattice parameters ratios and solid state NMR. Operando X-ray diffraction recorded during charge at C/2 reveal subtle differences between the samples (of different particle size, morphology and carbon-coating nature) in the crystallinity of the intermediate compositions formed within the $Na_3V_2(PO_4)_2F_3$ - $NaV_2(PO_4)_2F_3$ phase diagram. A new temperature-controlled operando cell allowed to determine this phase diagram at 0°C, mostly unchanged compared to that of recorded at 25°C. Very high charging and discharging rates are demonstrated and intermediate compositions could be spotted operando even up to 25 C rate at which the compositional phase diagram is only slightly altered compared to that recorded under equilibrium conditions. Optimized carbon-coated $Na_3V_2(PO_4)_2F_3$ shows exceptional rate and electrochemical cycling capabilities, as demonstrated by 18650 hard-carbon // $Na_3V_2(PO_4)_2F_3$ prototypes of 75 Wh/kg that could be charged-discharged 4000 times at 1C rate.

## 1. Introduction

The development of large scale electrical energy storage systems is the greatest challenge for the storage and the integration into the grid of renewable energies. Concerns about the availability and thus the prize of lithium sources [1] recently promoted an intense research activity towards Na-ion batteries, that rapidly became the most appealing short term alternative to Li-ion batteries.[2–4] Two families of compounds turn out to be promising on the positive electrode side: layered transition metal oxides of general formula $Na_xMO_2$ [5] and phosphate-based materials [6]. The latter have three-dimensional frameworks built of $MO_6$ octahedra and $PO_4$ tetrahedra that offer a large number of atomic arrangements and possible compositions. Layered oxides have concentrated considerable research efforts, [7–14] from the demonstration of the electrochemical sodium de-intercalation and re-intercalation in $Na_xCoO_2$ [15] to the release of a prototype Na-ion battery using an air-stable electrode $Na_{0.90}[Cu_{0.22}Fe_{0.30}Mn_{0.48}]O_2$ free of critical raw elements versus hard carbon. [16]

Polyanionic-based materials appear as promising alternatives to layered oxides despite the weight penalty generated inherently by the replacement of the anion $O^{2-}$ by the anionic group $PO_4^{3-}$. The sodium superionic conductors (called NASICON) of general formula $A_xMM'(PO_4)_3$ were the first ones to draw attention, among which $Na_3V^{III}_2(PO_4)_3$ was shown to be the most attractive with a reversible capacity of 120 mAh/g at an average potential of 3.4 V versus $Na^+/Na$ and the involvement of the $V^{III/IV}$ redox couple. [17,18] Among polyanionic materials, the most promising to date turns out to be sodium-vanadium fluorophosphate compositions $Na_3V_2(PO_4)_2F_{3-y}O_y$ where $y$ can vary from 0 to 2. [19–30] This whole range of compositions, from the $V^{III}$-rich one $Na_3V_2(PO_4)_2F_3$

($y = 0$) to the $V^{IV}$-rich one $Na_3(VO)_2(PO_4)_2F$ ($y = 2$), can exchange reversibly two $Na^+$ ions. For instance, $Na_3V_2(PO_4)_2F_3$ ($y = 0$) delivers a reversible capacity of 128 mAh/g at an average voltage close to 3.9 V versus $Na^+/Na$, corresponding to a high intrinsic energy density of 507 Wh/kg. [26,31,32] Note that this energy density is competitive with that delivered by $LiFePO_4$ in Li-ion batteries, and much higher than that delivered by the system just mentioned before, i.e. $Na_{0.90}[Cu_{0.22}Fe_{0.30}Mn_{0.48}]O_2$, which is limited to an energy density of 325 Wh/kg (with a reversible capacity of 100 mAh/g at an average voltage of 3.25V).

As demonstrated by some of us, [23] the stoichiometric compound $Na_3V^{III}_2(PO_4)_2F_3$ (y = 0) crystalizes in the *Amam* orthorhombic space group at room temperature. This structure is described in **Figure 1a** and consists of a three dimensional framework with $V_2O_8F_3$ bi-octahedra connected by $PO_4$ tetrahedra and of large tunnels where $Na^+$ ions are mobile upon extraction/insertion reactions. The structural evolution of $Na_{3-x}V_2(PO_4)_2F_3$ (x ≤ 2) has been extensively characterized *operando* during the electrochemical cycling of $Na//Na_3V_2(PO_4)_2F_3$ cells: the phase diagram stabilized within the composition range $Na_3V^{III}_2(PO_4)_2F_3$ – $Na_1V^{IV}_2(PO_4)_2F_3$ is a complex succession of biphasic and solid solution-type reactions as summarized in **Figure 1b.** [24] Recently we have also studied the impact of small amounts of oxygen defects on the structural, transport and electrochemical properties of $Na_3V_2(PO_4)_2F_{3-y}O_y$. [27] The structural framework remains similar to that of $Na_3V_2(PO_4)_2F_3$ but with an increasing disorder in the $Na^+$ ions distribution, changing from three to four crystallographic sites with increasing $y$. [27] The richer the content in oxygen the higher the electronic conductivity, in relation with the mixed valence state $V^{3+}/V^{4+}$ within the bi-octahedral units $V_2O_8F_{3-y}O_y$, and the easier the diffusion of $Na^+$ ions in these bare (*i.e.* not coated) $Na_3V_2(PO_4)_2F_{3-y}O_y$ type compounds. Nevertheless, we have also reported that

carbon-coated $Na_3V_2(PO_4)_2F_3$ shows excellent electrochemical performance at high rate, with only 20% loss of the capacity at 20C. [33]

In this paper, a series of three different samples of so-called NVPF materials (*i.e.* $Na_3V_2(PO_4)_2F_3$) are compared. They were obtained with different synthesis methods, either as bare NVPF powder (without any carbon coating), or as composites with carbon, either as carbon nanoparticles within the grain boundaries or as a conductive thin layer covering the particles. The impact of the microstructure (morphology of the particles, nature of the carbon coating) and of a small amount of oxygen defects will be discussed considering the structure of the material and its electrochemical performances in Na-ion batteries. Especially, changes within the phase diagram were carefully scrutinized *operando* (during the cycling of the battery) using Synchrotron X-ray diffraction, depending on the electrode formulation, cycling rate and temperature. From all these findings the most optimized material was thoroughly studied in "extreme" conditions, at low temperature and/or at high cycling rate, and in 18650 prototypes versus hard carbon.

## 2. Experimental

Polycrystalline samples of $Na_3V_2(PO_4)_2F_3$ (NVPF) were synthetized by three different synthesis routes, the three of them being two-step solid-state reactions. The first step consists in the synthesis of the vanadium phosphate ($VPO_4$) and the second step in the sintering under argon at 750 °C for 2 h (heating/cooling rate of 3 °C/min) of a stoichiometric mixture of $VPO_4$ and NaF (Sigma-Aldrich, $\leq$ 99%). The difference between the three synthesis routes lies in the nature of the vanadium phosphate used as a precursor and/or of the carbon coating:

- VPO$_4$, used as the precursor to obtain the bare Na$_3$V$_2$(PO$_4$)$_2$F$_3$ sample (called **bare NVPF** in the following), was prepared by mixing stoichiometric amounts of V$_2$O$_5$ (Sigma-Aldrich, $\geq$ 99.6 %) and NH$_4$H$_2$PO$_4$ (Sigma-Aldrich, $\geq$ 99.99 %) in a high energy ball miller for 90 min. This mixture was then continuously heated under Ar/H$_2$ (95%/5%) to ensure a complete reduction of V$^{V}$ to V$^{III}$ at 300 °C for 5 h (with a heating ramp of 0.5 °C/min) and at 800 °C for 5 h (with a heating ramp of 2 °C/min), before being cooled down to room temperature at 3 °C/min.

- A VPO$_4$ – carbon composite was used as a precursor to obtain a first carbon composite sample (called **C-VPO$_4$ NVPF** in the following). It was prepared by mixing stoichiometric amounts of V$_2$O$_5$ and (NH$_4$)$_2$HPO$_4$ with an excess of divided carbon soot (C$_{sp}$) as described in ref [34]. The role of Cs$_p$ is first to ensure the carbothermal reduction of vanadium from the oxidation state 5+ to 3+, and then to be a source of carbon for the formation of the composite C-VPO$_4$ with carbon nanoparticles in the grain boundaries. [23]

- VPO$_4$ used as a precursor for the formation of the carbon coated sample (called **coated NVPF** in the following), is the same as the one used to prepare the bare NVPF sample. The peculiarity of coated NVPF lies in the nature of its carbon coating, obtained as described in ref [34] from the decomposition of an organic compound. In that case, the covering of the particles and of the grain boundaries is homogeneous, as a thin layer.

Note that the partially oxidized bare composition Na$_3$V$_2$(PO$_4$)$_2$F$_{2.8}$O$_{0.2}$ (NVPF$_{2.8}$O$_{0.2}$), whose synthesis has been described elsewhere, [27] has been used for comparison. The chemical composition (stoichiometry in Na, V, P, i.e. within the accuracy equal to 3/2/2) of the three

synthesized samples was confirmed by inductively coupled plasma-optical emission spectroscopy (ICP-OES) using a Varian Model 720-ES spectrometer after complete dissolution of the powder into a hydrochloric acid (HCl) solution.

High angular resolution Synchrotron X-ray powder diffraction (SXRPD) data were collected using the powder diffractometer BL04-MSPD beamline of ALBA synchrotron (Barcelona, Spain). The powders were placed in a 0.5 mm diameter capillary and the data recorded in Debye-Scherrer geometry with wavelengths around 0.95 Å in the $2\theta$ angular range $1 - 70$ ° with an accumulation time of 6 minutes. For sake of clarity, due to differences in wavelengths, the comparison of the SXRD patterns has been done using Q range (Å$^{-1}$). Diffraction data treatment was performed using the FullProf Suite. [35]

$^{23}$Na magic angle spinning nuclear magnetic resonance (MAS NMR) spectra were recorded on a Bruker Avance 500 MHz spectrometer (132.3 MHz resonance frequency for $^{23}$Na) using a standard Bruker 2.5 mm MAS probe with a 30 kHz typical spinning frequency. A short pulse length of 1 μs corresponding to a selective $\pi/12$ pulse determined using an aqueous 0.1 mol/L NaCl solution was employed. The spectral width was set to 1 MHz and the recycle time to $D_0 = 0.5$ s, long enough to avoid T1 saturation effects. The baseline distortions resulting from the spectrometer dead time (5-10 μs) were removed computationally using a polynomial baseline correction routine. The 0 ppm external reference was a 0.1M NaCl aqueous solution. $^{31}$P MAS NMR spectra were recorded on a Bruker Avance III 100 MHz spectrometer (40.6 MHz resonance frequency for $^{31}$P), using a standard Bruker 2.5 mm MAS probe with a 30 kHz typical spinning frequency. A Hahn echo

sequence was used with a 90 ° pulse of 1.1 μs. A recycle delay of 1 s was typically used. The 0 ppm external reference was $H_3PO_4$ 85 % sigma Aldrich.

Scanning electron microscopy (SEM) analysis of metallized samples (Pd-deposited) was performed using a Hitachi Model S-4500 microscope.

*Operando* SXRPD data were collected on the beamline BL04-MSPD at ALBA using a transmission *in situ* electrochemical cell already described in details elsewhere. [36] The sodium battery was obtained from the stacking of the positive electrode, glass fiber separators (Whatman) wetted with a 1 M solution of $NaPF_6$ (Strem Chemical; 99%) in a mixture of ethylene carbonate and dimethyl carbonate (EC:DMC = 1:1) and sodium metal as the counter electrode. The internal pressure within the cell was applied through a spring to ensure an optimal electrical contact. This stacking was inserted between two beryllium windows acting as X-ray-transparent current collectors. The electrochemical behavior and the corresponding phase diagram were studied using different electrode formulations (relative percentages of the active material, carbon conductive additive and polytetrafluoroethylene binder within the electrode), different cycling rates (C/n with n corresponding to the exchange of 2 $Na^+$ in n hours) and different electrochemical cycling temperatures (0°C versus 25°C). The *in situ* cell was cooled down using an external serpentine fixed at the height of the electrochemical stacking and the effective temperature of the sample was estimated from the comparison of its cell parameters with those of NVPF as a function of the temperature. For the micro-diffraction experiment performed on the BL04-MSPD beamline, the data were collected at the Sn K-edge wavelength ($\lambda = 0.4246$ Å), with 2 s of effective integration time using a 2 dimensional (2D) Rayonix CCD165 detector. The detector was positioned at 445mm

from the sample, hence avoiding the strong Bragg peaks of the Be windows, but allowing to cover down to 2Å d-spacing, which is sufficient for accessing the most relevant (110)/(002) and (220)/(113) group of reflections characteristic of NVPF. 2D to 1D azimuthal integrations were performed using the Fit2D software while masking strong spots arising from the sodium foil used as negative electrode. The background induced by the electrolyte, the carbon and the cell was modelled for the first pattern collected for each rate and position, it was then subtracted from all successive data.

Cyclability and rate capability electrochemical tests were performed in full cells versus hard carbon, either in coin cells or in 18650 cells. The positive electrode contained 91 wt.% active material and the loading was 12 mg/cm$^2$ for the cyclability tests and 6 mg/cm$^2$ for the rate capability tests, whereas the hard carbon negative electrode contained 92 wt.% active material and 6 mg/cm$^2$ and 3 mg/cm$^2$ respectively. Both electrodes were double side coated on aluminum foil using a roll to roll machine with PVDF binder. After a drying overnight under vacuum, the electrodes were slitted and calendared to 35% porosity, then wound together with a standard tri-layer polypropylene polyethylene separator. Finally the jelly rolls were filled with EC/DMC (1/1) NaPF$_6$ 1M electrolyte. Cycle life was carried out at constant current between 2 and 4.25V at room temperature. Discharge rate capability test was evaluated using slow rate C/5 charge up to 4.25V and increasing discharge rate from C/10 to 150C down to 2V, while charge rate capability was tested the opposite way up to 40C.

## 3. Results

## 3.1. Pristine materials

The SXRPD patterns of the three NVPF samples obtained and discussed in this paper are compared in **Figure 2**. All the main diffraction lines can be indexed in unit cells described in the *Amam* space group as determined previously for $Na_3V_2(PO_4)_2F_3$. [23] Close inspection of the SXRD data shows small shifts towards higher Q values as well as a slight right asymmetry for all the *l*-dependent reflections for the sample C-VPO$_4$ NVPF, highlighting a lower *c* cell parameter which is the propagation direction of the bi-octahedral units $V_2O_8F_3$, and thus very sensitive to the presence of oxygen defects. A comparison of all the cell parameters determined from the structural Rietveld refinements is given in **Table 1**. It confirms the lower *c* cell parameter for the C-VPO$_4$ NVPF sample, and thus a volume cell of 877.778(1) $Å^3$ vs. 878.066(1) and 878.389(1) $Å^3$ for the coated and bare NVPF samples respectively. As already discussed in [27], oxygen substitution for fluorine in $Na_3V_2(PO_4)_2F_{3-y}O_y$ can easily be detected from the close comparison of their cell unit-cell parameters and volumes. Nevertheless, here, a variation of less than 0.1% is observed suggesting the presence of localized defects but in very small quantities. Note that the b/a ratio (i.e. the parameter sensitive to the orthorhombic distortion induced by the distribution of the Na$^+$ ions within the channels) is similar for the three phases, close to 1.0016.

Solid-state MAS NMR was identified as being extremely sensitive to oxygen defects in vanadium fluoride phosphate materials (LiVPO$_4$F [29] and $Na_3V_2(PO_4)_3F_3$ [27]). Besides the SXRD data analysis, the NMR spectra are thus displayed in **Figure 3** with their main signals at 138 ppm for $^{23}$Na NMR and at 6097 ppm for $^{31}$P NMR. These features are associated with Na$^+$ ions located in the direct vicinity of $V^{III}_2O_8F_3$ bi-octahedral units and with P$^{5+}$ ions in interaction with four

$V^{III}O_4F_2$ octahedra sharing one oxygen with $PO_4$, respectively. As previously reported, [27] the appearance of additional signals below 120 ppm for $^{23}Na$ NMR and 5000 ppm for $^{31}P$ NMR is caused by the presence of $V^{IV}$ defects in $Na_3V_2(PO_4)_2F_3$: the more $V^{4+}$ in the vicinity of the probed nucleus, the more shifted to lower chemical shifts the signals are observed. They can be ascribed to a partial oxidation of $V^{III}$ to $V^{IV}$ as a charge compensation for the presence of oxygen defects ($O^{2-}$) in substitution for fluorine ($F^-$).[27] The NMR spectrum of the oxidized material $Na_3V_2(PO_4)_2F_{2.8}O_{0.2}$, with 10% of vanadium at the tetravalent state as vanadyle-type defects, is given for comparison. It is clearly much more oxidized than the three NVPF samples studied in this paper, with higher intensities for the signals associated to the mixed valence environments $V^{3+}$-$V^{4+}$ and smaller intensities for the $V^{3+}$ only environments. In very good agreement with the analysis of the cell parameters, the C-VPO$_4$ NVPF sample is the one which presents the "highest" amount of defects among the three NVPF samples, whereas the bare NVPF and coated NVPF samples are very similar in cationic and anionic compositions.

**Figure 4** displays scanning electron micrographs of bare NVPF, C-VPO$_4$ NVPF and coated NVPF. Bare NVPF is characterized by particles of 300 nm in size in average, C-VPO$_4$ NVPF by a few micrometer sized particles with carbon nanoparticles in the grain boundaries, and coated NVPF by 100 to 500 nm sized particles with a homogeneous carbon coating at their surface.

### 3.2. Changes in the phase diagram observed upon cycling at a rate of C/2

In order to precisely compare the electrochemical behavior of the three $Na_3V_2(PO_4)_2F_3$ samples, *operando* SXRPD patterns have been collected during a charge performed at a rate of C/2, and are

compared in **Figure 5**. The corresponding electrochemical data are given in **Figure 6**. The overall evolution of the SXRPD patterns upon $Na^+$ deintercalation from $Na_3V_2(PO_4)_2F_3$ is nearly the same for the three samples and essentially similar to that previously reported. [24] Starting from $Na_3V^{III}_2(PO_4)_2F_3$ ($Na_3VPF$) the sodium extraction leads to a succession of reactions involving all the key compositions mentioned in **Figure 1b**, with the formation of the end-member $Na_1V^{IV}_2(PO_4)_2F_3$ ($Na_1VPF$) at the end of charge for $V_{max} = 4.4$ V. As highlighted in **Figure 7** the orthorhombic splitting between the (200) and (020) diffraction peaks characteristic of the composition $Na_{2.4}VPF$ is clearly visible for the bare NVPF and coated NVPF samples, whereas only a significant broadening of these lines is observed for C-VPO$_4$ NVPF. This suggests that at this C/2 rate the corresponding alkali and/or charge ordering cannot be properly established within large and non-coated particles of C-VPO$_4$ NVPF for which the diffusion length is larger and electronic percolation limited.

The key SXRPD patterns shown in **Figure 7** were analyzed by Rietveld refinements while examples of such refinements are given in supplementary information in **Figure S1**. The cell parameters determined for the representative intermediate phases $Na_xVPO_4F$ (x = 2.4, 2 and 1) are gathered and compared in **Table 1**. As expected, there is a continuous decrease of the cell volume (V/Z) upon $Na^+$ extraction as the vanadium transition metal ion is oxidized for charge compensation. Its first coordination sphere VO$_4$F$_2$ is thus contracted thanks to the stronger covalency of the V-O(F) bonds. Furthermore, the comparison with the results reported in reference [24] reveals that the compositions we associate to $Na_2VPF$ and $Na_1VPF$ are very close to the compositions expected with a deviation being less than 0.27 and 0.18 % respectively. Since the main difference between these three samples lies in the $Na_{2.4}VPF$ composition that displays an

almost extinguished orthorhombic distortion for the C-VPO$_4$ NVPF sample (i.e. b/a = 1.002, vs. 1.008 for bare NVPF and 1.006 for coated NVPF) (**Figure 7** and **Table 1**), the big size of the particles appears to be more limiting for the kinetics of the reaction than the electronic percolation. In the following, as being the most affected by the kinetics of the reaction, only the composition range $2 \leq x \leq 3$ in the various Na$_x$VPF samples will be discussed in details. Indeed, as in the composition range $1 \leq x \leq 2$ Na$^+$ deintercalation occurs mainly as a solid solution reaction, it is as expected less sensitive to the kinetics.

In order to visualize the impact of a small oxygen substitution for fluorine, **Figure 8** shows a comparison of the phase diagrams observed upon Na$^+$ de-intercalation from the samples C-VPO$_4$ NVPF (the most oxidized as seen from NMR) and bare NVPF$_{2.8}$O$_{0.2}$ at a cycling rate of C/2. As highlighted, C-VPO$_4$ NVPF allows to deintercalate towards clearly identified Na$_{2.4}$VPF and Na$_{2.2}$VPF compositions, showing three well-defined biphasic reactions, successively between Na$_3$VPF, Na$_{2.4}$VPF, Na$_{2.2}$VPF and Na$_2$VPF (note that the orthorhombic distortion is almost not observed for Na$_{2.4}$VPF).

For the oxygen substituted material, Na$_3$VPF$_{2.8}$O$_{0.2}$, the phase diagram observed upon Na$^+$ deintercalation is clearly different: it undergoes a biphasic domain between Na$_3$VPF$_{2.8}$O$_{0.2}$ and Na$_{3-x}$VPF$_{2.8}$O$_{0.2}$ ($0 \leq x \leq x_1$), a solid solution domain for $x_1 \leq x \leq x_2$ and a biphasic domain between Na$_{3-x}$VPF$_{2.8}$O$_{0.2}$ and Na$_2$VPF$_{2.8}$O$_{0.2}$ ($x_2 \leq x \leq 1$). The progressive shift of the (200) reflection ascribed to a Na$_{3-x}$VPF$_{2.8}$O$_{0.2}$ solid solution and its significant broadening (**Figure 8b**) suggest the continuous evolution of the charge/alkali ordering and the existence of locally-ordered crystalline domains, very limited in size. This tends to minimize the electrostatic repulsions and the strains

induced by the progressive formation of vanadyle-type bonds in relation with the oxidation of $V^{3+}$ to $V^{4+}$ in the oxidized phase. In fact the solid solution could be rather seen/described as a series of phases close in structure and in composition that evolve together towards the same $Na_2VPF_{2.8}O_{0.2}$ target, which is the composition corresponding to the deintercalation of 1 $Na^+$ per formula unit. As displayed in **Figure S2,** pattern #21 that corresponds to an average composition $Na_{\sim2.67}VPF_{2.8}O_{0.2}$ can be refined by the Rietveld method from a two-phase model: the first and main one is the pristine composition $Na_3VPF_{2.8}O_{0.2}$ (60%); the second one is found to be $Na_{2.4(1)}VPF_{2.8}O_{0.2}$ (40%). Whereas the structure of $Na_3VPF_{2.8}O_{0.2}$ is described in an orthorhombic unit cell (*Amam*, with a small distortion such as a/b = 1.001), [27] the structure of the de-intercalated phase is described in a tetragonal unit cell (*I4/mmm*) similar to that stabilized for $Na_3V_2(PO_4)_2F_3$ above 400K, [23] with cell parameters $a = 6.3710(2)$ Å and $c = 10.7522(3)$ Å and a distribution of the $Na^+$ ions on a ring within the tunnels of the host structure. These cell parameters evolve down to $a = 6.3502(2)$ Å and up to $c = 10.7572(3)$ Å (pattern #51) in the solid solution domain $Na_{3-x}VPF_{2.8}O_{0.2}$, with a $c$ parameter expansion of 0.05% concomitant with a basal plane contraction of 0.65% in agreement with previous observations made on $Na_3V_2(PO_4)_2F_3$ and other related phases. [24,37] Beyond the pattern #51 the growth of the intermediate phase $Na_2VPF_{2.8}O_{0.2}$ is observed concomitantly with the voltage step observed in the electrochemical curve and corresponding to the transition between the first voltage domain at 3.75 V vs. $Na^+$/Na and the second at 4.2 V.

As highlighted in **Figure 7**, the phase diagram observed for the C-VPO$_4$ NVPF sample around the composition $Na_{2.4}VPF$ is thus closer to that determined for the partially oxygen substituted phase $Na_{3-x}VPF_{2.8}O_{0.2}$ than to that determined for the bare and coated NVPF compounds. Indeed, the

presence of small amounts of oxygen defects induces locally, for charge compensation, the oxidation of $V^{3+}$ to $V^{4+}$ ions, and thus the formation of strong covalent vanadyle type bonds $\{V=O\}^{2+}$, very short versus the $V^{3+}$-F bonds observed along the bi-octahedral units. These defects obviously prevent the formation of the charge and/or cation ordering required to stabilize the intermediate phase $Na_{2.4}VPF$, which corresponds to an average oxidation state around +3.25 and thus to an ordering between $3V^{III}:1V^{IV}$. The defects limit the extension of the ordered domains, in good agreement with the global broadening of the diffraction lines and with the almost disappearance of the orthorhombic distortion (b/a = 0.998 versus 0.992 and 0.994 for the bare and coated NVPF compounds respectively). Oxygen and vanadyle-type defects have thus a significant impact on the phase diagram stabilized upon sodium deintercalation from NVPF, with the disappearance of the intermediate phases and the associated bi-phased reactions, to the benefit of a solid solution type reaction. Note that changes in the structural mechanism observed upon cycling have also been observed for the $V^{IV}$-rich $Na_3V_{2-y}(VO)_y(PO_4)_2F_{3-y}$ composition ($y \cong 2$) depending on the concentration of $V^{III}$ defects in the $V^{IV}$-rich compound. [38, 39]

Beside the impact of oxygen defects on the phase diagram, it is also interesting to highlight the influence of the carbon coating. From this point of view, pristine bare and coated NVPF samples can be compared since they have similar diffraction peak shapes (**Figure 2**), similar structure and negligible amounts of oxygen defects. Despite these similarities, they exhibit small differences upon $Na^+$ deintercalation as shown in **Figure 5** and **Figure 7.** As already discussed, the first one is bare (i.e. without any carbon coating) and the second one is such that the active compound is covered by a thin layer of carbon at the surface of the primary particles. Here no difference is observed regarding the symmetry of the stabilized phases. For instance the orthorhombic split is

clearly observed (**Figure 7**). However, a significant difference is seen in the widths of the diffraction lines observed for the bare NVPF, which tends to indicate that the crystalline coherent domains were reduced, despite they were similar, in their pristine state, to the coated NVPF. A carbon coating allows to significantly improve the electrochemical performance as it was demonstrated for $LiFePO_4$ [40] and more recently for $Na_3V_2(PO_4)_3$ [41-42]: a thin conductive layer leads to an easier diffusion of the electrons and thus of the alkali ions within the whole electrode, and thus to a decrease of the internal resistance and to a reaction closer to the equilibrium with extended crystalline and ordered domains.

### 3.3. Performance of the optimized coated NVPF

As just discussed and revealed by an in-depth comparison of three NVPF samples, the control of the amount of oxygen defects and of the nature of the composite *carbon - active material* is essential for an optimization of the transport properties, and thus for the fast stabilization of the complex phase diagram which consists in a succession of phase transitions implying either alkali or charge ordering. In the following, we report on the impact of cycling in extreme conditions (low temperature, very high rate) on the phase diagram. We will demonstrate that a well optimized NVPF sample shows excellent transport properties and make it a material of choice for batteries operating at low temperature and in high rate (power) conditions. This will be also demonstrated within 18650 prototypes, in excellent agreements with results already obtained a few years ago by some of us in laboratory full cells versus hard carbon. [33]

*3.3.1. Impact of extreme conditions on the phase diagram*

The Coated NVPF sample has been tested in extreme conditions such as low temperature (at ~ 0°C) and high cycling rate (from C/10 to 25C, through 5C), in order to evaluate the impact of these parameters on both the phase diagram and the electrochemical behavior. The first electrochemical cycles obtained in different conditions for Na//coated NVPF cells are gathered and compared in **Figure 9**. First, *operando* experiments have been carried out at low temperature in the *in situ* electrochemical cell developed and modified by Leriche et al. [36] that was cooled down with a conventional antifreeze agent refrigerated at -10 °C. Due to heat dissipation in the whole line from the chiller to the cell and through the cell stainless steel body, the actual temperature within the battery was estimated to be near 0°C. The electrochemical performance obtained at C/10, at room temperature (RT) and at low temperature (~ 0°C), are very close to each other, with no extra polarization resistance for the battery cycled at low temperature despite a higher irreversible capacity at the end of the first cycle. Moreover, the SXRPD patterns recorded upon cycling at low temperature indicate that the phase diagram remains unchanged as displayed in **Figure 10**. The cell parameters determined for the intermediate phases $Na_{2.4}VPF$, $Na_2VPF$ and $Na_1VPF$ are given in **Table S1** for comparison with those determined at RT for the same material, i.e. coated NVPF. As expected, a contraction of the unit cells is observed, but very limited (less than 0.04%) all along the $Na^+$ deintercalation from the structure. The orthorhombic distortion tends to slightly increase, up to 0.09 %. The results of this experiment performed at low temperature highlight again that the mobility of $Na^+$ ions is very fast in these materials, [28] with the ability to stabilize attractive performance at low temperature.

In order to check for the stability of the phase diagram upon cycling at very different rates, from low rates at C/10 to very high rates at 25C, the electrode formulation was modified. To prevent possible heterogeneity due to limited electronic percolation within the electrode for experiments performed at 5C and 25C, the proportion of carbon conductive additive was increased to 55 wt.% for 35 wt.% of active material and 10 wt.% of PTFE as binder. The corresponding electrochemical data are given in **Figure 9**, in comparison with those obtained at C/10, either at RT or at ~0°C. The first cycle obtained at 5C is very similar to that obtained at C/10. It demonstrates the ability of the optimized coated NVPF to deliver an attractive reversible capacity of ~105 mAh/g within 12 mins. Obviously, higher polarization and thus lower reversible capacity are observed at a charge rate of 25C, but only 15% of the capacity is lost. **Figure 11** compares two sets of XRD data collected while charging the electrochemical cell at 5C (charge in 12 mins and 12 s per pattern) and at 25C (charge in 2 mins 24 s and 5 s per pattern). It can be noticed that the intermediate member $Na_2VPF$ is also clearly identified at the voltage step between the two domains or just after at high rates, whereas $Na_1VPF$ is unambiguously identified through the diffraction line (220) at 17.63°. Once again the main differences are observed in the composition range between $Na_3VPF$ and $Na_2VPF$ since the intermediate phases corresponding to alkali and charge orderings are not stabilized in conditions far from the equilibrium. Nevertheless, as revealed by the galvanostatic intermittent titration technique-like experiment shown in **Figure 12**, the intermediate ordered phases can be recovered as soon as the relaxation is long enough (here 20 mins) for the system to reach the equilibrium. Approximatively a thousand of SXRPD patterns have been collected between $Na_3VPF$ and $Na_2VPF$ which reveal that the system, even if strongly exposed to non-equilibrium conditions can stabilize a phase diagram exactly identical to the one previously observed at lower rates. This high rate diffusion ability and stability of the phase diagram are also in good agreement

with the absence of metastable phases previously observed for the olivine $LiFePO_4$ (LFP) in Lithium-ion batteries cycled at high rate. [43,44] In the case of LFP, lithium deintercalation occurs according to a bi-phasic reaction and the solubility limits change at high cycling rates, by-passing the first-order phase transition between the end-members $LiFePO_4$ and $FePO_4$ with the formation of an intermediate phase close in composition to $Li_{2/3}FePO_4$. In the case of coated NVPF, we did not observe such phenomena, showing the ability of NVPF to reach its equilibrium upon cycling even at high rates.

One issue when collecting *operando* diffraction, spectroscopy or real space imaging data, especially at very high cycling rates, is the possibility for spatial heterogeneities. In that case, different parts of the electrode may behave differently and the part studied (i.e. irradiated by the beam) can be not representative of the overall sample due to a state of charge or of discharge different from the average. Such an inhomogeneous behavior has already been reported for XAS experiments performed at a rather low rate of 1C for the system $Li//LiFePO_4$. [36,45] It was thus worth to check that point, considering especially that we did consider cycling rates as high as 25C in electrochemical cells similar to those used in [45]. All the SXRPD patterns presented here were collected with the detector MYTHEN on a 2mm x 0.7mm area of the electrode corresponding to the size of the beam. A 10 degrees oscillation around the direction of the beam further contributes to improve the averaging of the sample probed (surface and bulk). In order to track for possible spatial inhomogeneity during cycling, similar experiments were performed on the High Pressure/ MicroDiffraction station of the BL04-MSPD beamline. In that case, the X-ray beam was focused down to 20 μm x 20 μm and the powder diffraction patterns were collected using a 2D detector. For different cycling rates (as shown here in **Figure 13** for C, 10C and 20C rates), SXRPD patterns

were collected at three positions of the electrode separated by 1mm, which correspond thus to the central and extreme positions of the standard experiments just mentioned. The comparison of these data allow to discriminate between an SXRPD pattern being representative of an average due to heterogeneity and an SXRPD pattern being representative of all the parts of the electrode. As highlighted in **Figure 13** this experiment demonstrates that the three probed regions exhibit the same state of Na deintercalation for all measured rates. Typically, the characteristic feature of the $Na_{2.4}V_2(PO_4)_2F_3$ phase is observed, as well as the "crossing" between the (220) and (113) Bragg reflections, at exactly the same voltage. Hence beam-induced artefacts or unequal pressures within the cell can be ruled out, and this micro-diffraction experiment reveals that all the results presented here are representative of the global electrode.

*3.3.2. Electrochemical performance in 18650 prototypes versus hard carbon*

These very attractive results motivated the preparation of 18650 industry representative cells aimed at testing the ability of NVPF materials to sustain long cycle life and high cycling rates. **Figure S3** given in supplementary information shows the first cycle of a full Na-ion coin cell, with hard carbon at the negative electrode and the optimized coated NVPF at the positive electrode. The electrochemical cycling was performed in the potential window 2 - 4.3 V, yielding a first charge capacity of ~130 mAh/g in good agreement with the theoretical capacity corresponding to the exchange of 2 $Na^+$ per formula unit. The reversible capacity is then close to 100 mAh/g at an average potential of 3.4 V. Note that the comparison with a full Na-ion coin cell made with hard carbon at the negative electrode and C-VPO$_4$ NVPF at the positive electrode reveals again the

better performance of the coated compound, with a higher first charge capacity, a higher discharge capacity and a smaller irreversible capacity at the end of the first cycle.

The performance obtained in 18650 cells are given in **Figure 14**. **Figure 14a** reveals first that a long term cyclability can be demonstrated at a 1C rate upon charge and discharge for a first batch of prototypes (higher loading, obtained energy density of 75 Wh/kg). Over 3750 cycles were performed in the potential window 2 – 4.25 V (100% of depth of discharge) before reaching the limit of 20% capacity loss. This result compares favorably with best state of the art Li-ion technology. Then, as shown in **Figure 14b**, the rate capabilities were tested in a second batch of prototypes (lower loading, obtained energy density of 55 Wh/kg) with discharge and charge rates ranging between C/2 to 150C, i.e. from 2h to 24s. Interestingly, outstanding capacity retentions were observed even at very high rates: more than 75% of the capacity is recovered up to 10C (i.e. 6 mins) in charge and up to 100C (i.e. 36 s) in discharge. At this rate and taking into account an average discharge voltage of 2.55 V the power cell achieves more than 3.8 kW/kg continuous power in discharge. These first results on un-optimized cells are very encouraging for the technology. These experiments reveal thus that $Na^+$ ions diffusion is significantly faster in discharge than in charge, both being fast (as highlighted in **Figure S4**) . Coated NVPF appears thus as an already very much optimized material for high power density Na-ion cells.

## 4. Conclusion

The comparison of three $Na_3V_2(PO_4)_2F_3$ samples, prepared according to different synthesis routes and with or without carbon coating, has demonstrated that despite subtle differences between them

(morphology and nature of the carbon coating, amount of oxygen defects) the phase diagram observed during Na$^+$ extraction is only slightly altered at moderate cycling rates (here C/2). An optimized carbon-coated Na$_3$V$_2$(PO$_4$)$_2$F$_3$ was shown to deliver promising electrochemical performance in *in situ* electrochemical cells, at room temperature and at 0°C, at very high rates (up to 25C), with no major loss of reversible capacity and no significant modification of the phase diagram observed within the composition range Na$_3$V$_2$(PO$_4$)$_2$F$_3$ - Na$_1$V$_2$(PO$_4$)$_2$F$_3$. 18650 prototypes of 75 Wh/kg, Na$_3$V$_2$(PO$_4$)$_2$F$_3$ versus hard-carbon, have demonstrated exceptional rate and electrochemical cycling capabilities with 4000 charge and discharge cycles performed at 1C rate. New progress is quickly expected, for instance with the optimization of the electrolyte and electrode formulation. Indeed, the appealing results presented in this paper were obtained in non-optimized cells.

**Supporting information**

Supporting information is available from the Wiley Online Library.

## References

[1]  J. M. Tarascon, *Nat. Chem.* **2010**, *2*, 510.

[2]  P. Johansson, P. Rozier, M. R. Palacín, M. in *Prospects for Li-ion Batteries and Emerging Energy Electrochemical Systems. Series on Chemistry, Energy and the Environment.* (Eds: L. Monconduit, L. Croguennec, K. M. Kadish, R. Guilard), World Scientific Publishing Co Pte Ltd **2018**, Ch. 4.

[3]  N. Yabuuchi, K. Kubota, M. Dahbi, S. Komaba, *Chemical Reviews* **2014,** *114* (23), 11636.

[4]  C. Delmas, Adv. Ener. Mat., **2018**, *8*, 1703137.

[5]  M. Huon Han, E. Gonzalo, G. Singh, T. Rojo, *Energy Environ. Sci.* **2015**, *8*, 81.

[6]  C. Masquelier, L. Croguennec, *Chem. Rev.* **2013**, *113*, 6552.

[7]  D. Kim, E. Lee, M. Slater, W. Lu, S. Rood, C. S. Johnson, *Electrochem. Commun.* **2012**, *18*, 66.

[8]  S. Komaba, N. Yabuuchi, T. Nakayama, A. Ogata, T. Ishikawa, I. Nakai, *Inorg. Chem.* **2012**, *51*, 6211.

[9]  N. Yabuuchi, M. Kajiyama, J. Iwatate, H. Nishikawa, S. Hitomi, R. Okuyama, R. Usui, Y. Yamada, S. Komaba, *Nat. Mater.* **2012**, *11*, 512.

[10] M. Sathiya, K. Hemalatha, K. Ramesha, J. M. Tarascon, A. S. Prakash, *Chem. Mater.* **2012**, *24*, 1846.

[11] J. Billaud, G. Singh, A. R. Armstrong, E. Gonzalo, V. Roddatis, M. Armand, T. Rojo, P. G. Bruce, *Energy Env. Sci* **2014**, *7*, 1387.

[12] N. Yabuuchi, R. Hara, K. Kubota, J. Paulsen, S. Kumakura, S. Komaba, *J Mater Chem A* **2014**, *2*, 16851.

[13] D. Carlier, J. H. Cheng, R. Berthelot, M. Guignard, M. Yoncheva, R. Stoyanova, B. J. Hwang, C. Delmas, *Dalton Trans.* **2011**, *40*, 9306.

[14] R. Berthelot, D. Carlier, C. Delmas, *Nat. Mater.* **2011**, *10*, 74.

[15] C. Delmas, J.-J. Braconnier, C. Fouassier, P. Hagenmuller, *Solid State Ion.* **1981**, *3-4*, 165.

[16] L. Mu, S. Xu, Y. Li, Y.-S. Hu, H. Li, L. Chen, X. Huang, *Adv. Mater.* **2015**, *27*, 6928.

[17] S. Y. Lim, H. Kim, R. A. Shakoor, Y. Jung, J. W. Choi, *J. Electrochem. Soc.* **2012**, *159*, A1393.

[18] F. Lalère, J. B. Leriche, M. Courty, S. Boulineau, V. Viallet, C. Masquelier, V. Seznec, *J. Power Sources* **2014**, *247*, 975.

[19] P. Serras, V. Palomares, A. Goñi, I. Gil de Muro, P. Kubiak, L. Lezama, T. Rojo, *J. Mater. Chem.* **2012**, *22*, 22301.

[20] P. Serras, V. Palomares, A. Goñi, P. Kubiak, T. Rojo, *J. Power Sources* **2013**, *241*, 56.

[21] Y.-U. Park, D.-H. Seo, H.-S. Kwon, B. Kim, J. Kim, H. Kim, I. Kim, H.-I. Yoo, K. Kang, *J. Am. Chem. Soc.* **2013**, *135*, 13870.

[22] Y.-U. Park, D.-H. Seo, H. Kim, J. Kim, S. Lee, B. Kim, K. Kang, *Adv. Funct. Mater.* **2014**, *24*, 4603.

[23] M. Bianchini, N. Brisset, F. Fauth, F. Weill, E. Elkaim, E. Suard, C. Masquelier, L. Croguennec, *Chem. Mater.* **2014**, *26*, 4238.

[24] M. Bianchini, F. Fauth, N. Brisset, F. Weill, E. Suard, C. Masquelier, L. Croguennec, *Chem. Mater.* **2015**, *27*, 3009.

[25] A. A. Tsirlin, R. Nath, A. M. Abakumov, Y. Furukawa, D. C. Johnston, M. Hemmida, H.-A. Krug von Nidda, A. Loidl, C. Geibel, H. Rosner, *Phys. Rev. B* **2011**, *84*, 014429-1.

[26] R. Gover, A. Bryan, P. Burns, J. Barker, *Solid State Ion.* **2006**, *177*, 1495.

[27] T. Broux, T. Bamine, F. Fauth, L. Simonelli, W. Olszewski, C. Marini, M. Ménétrier, D. Carlier, C. Masquelier, L. Croguennec, *Chem. Mater.* **2016**, *28*, 7683.

[28] T. Broux, B. Fleutot, R. David, A. Brüll, P. Veber, F. Fauth, M. Courty, L. Croguennec, C. Masquelier, *Chem. Mater.* **2018**, *30*, 358.

[29] R. J. Messinger, M. Ménétrier, E. Salager, A. Boulineau, M. Duttine, D. Carlier, J.-M. Ateba Mba, L. Croguennec, C. Masquelier, D. Massiot, M. Deschamps, *Chem. Mater.* **2015**, *27*, 5212.

[30] T. Bamine, E. Boivin, F. Boucher, R. J. Messinger, E. Salager, M. Deschamps, C. Masquelier, L. Croguennec, M. Ménétrier, D. Carlier, *J. Phys. Chem. C* **2017**, *121*, 3219.

[31] J. Barker, R. K. B. Gover, P. Burns, A. J. Bryan, *Electrochem. Solid-State Lett.* **2006**, *9*, A190.

[32] J. Barker, R. K. B. Gover, P. Burns, A. J. Bryan, *J. Electrochem. Soc.* **2007**, *154*, A882.

[33] A. Ponrouch, R. Dedryvère, D. Monti, A. E. Demet, J.-M. Ateba Mba, L. Croguennec, C. Masquelier, P. Johansson, M. R. Palacín, *Energy Environ. Sci.* **2013**, *6*, 2361.

[34] N. Hall (CEA), S. Boulineau (CNRS), S. Launois (CEA), L. Simonin (CEA), L. Croguennec (CNRS), C. Masquelier (UPJV), *Patent priority n° FR1559709*, **2016**.

[35] J. Rodríguez-Carvajal, *Phys. B Condens. Matter* **1993**, *192*, 55.

[36] J.-B. Leriche, S. Hamelet, J. Shu, M. Morcrette, C. Masquelier, G. Ouvrard, M. Zerrouki, P. Soudan, S. Belin, E. Elkaïm, F. Baudelet, *J. Electrochem. Soc.* **2010**, *157*, A606.

[37] P. Serras, V. Palomares, J. Alonso, N. Sharma, J. M. López del Amo, P. Kubiak, M. L. Fdez-Gubieda, T. Rojo, *Chem. Mater.* **2013**, *25*, 4917.

[38] P. Serras, V. Palomares, T. Rojo, H. E. A. Brand, N. Sharma, *J. Mater. Chem.* **2014**, *2*, 7766.

[39] N. Sharma, P. Serras, V. Palomares, H. E. A. Brand, J. Alonso, P. Kubiak, M. L. Fdez-Gubieda, T. Rojo, *Chem. Mater.* **2014**, *26*, 3391.

[40] M. Armand, M. Gauthier, J.-F. Magnan, N. Ravet, *Patent priority n°CA2423129C*, **2016**.

[41] H. Li, C. Wu, Y. Bai, F. Wu, M. Wang, *J. Power Sources* **2016**, *326*, 14.

[42] Q. Ni, Y. Bai, F. Wu, C. Wu, *Adv. Science* **2017**, 1600275

[43] Y. Orikasa, T. Maeda, Y. Koyama, H. Murayama, K. Fukuda, H. Tanida, H. Arai, E. Matsubara, Y. Uchimoto, Z. Ogumi, *J. Am. Chem. Soc.* **2013**, *135*, 5497.

[44] H. Liu, F. C. Strobridge, O. J. Borkiewicz, K. M. Wiaderek, K; W. Chapman, P. J. Chupas, C. P. Grey, *Science* **2014**, *344*, 1252817.

[45] M. Zerrouki, G. Ouvrard, P. Soudan, B. Lestriez, C. Masquelier, M. Morcrette, S. Hamelet, J. Lesage, S. Belin, A. M. Flanck, F. Baudelet, *J. Power Sources* **2012**, 16.

**Figure 1**: Adapted and reproduced with permissions rom refs [23] and [24]. 2018 ACS a) On the left, the three dimensional framework of $NVPF_{3-y}O_y$ where the dark blue atoms emphasize the substitution site of oxygen for fluorine. In red are highlighted the (*a,b*) planes where the $Na^+$ ions are contained. On the right, distribution of the $Na^+$ ions assuming a small amount of oxygen defects, the fraction of filling in red of the Na atom highlights the partial occupancy of the crystallographic site. b) The potential-composition electrochemical curves obtained upon $Na^+$ extraction from $Na_3V_2(PO_4)_2F_3$ (NVPF). The first cell was cycled (GITT) between the compositions $Na_3VPF$ and $Na_2VPF$; the second one (galvanostatic cycling) between the compositions $Na_2VPF$ and $Na_1VPF$. Single-phase compositions are highlighted by colored circles.



**(a) Structure of $Na_3V_2(PO_4)_2F_{3-y}O_y$ with y ≈ 0**

F

$PO_4$

$Na^+$ containing plane

F (or O defect)

$V_2O_8F_{3-y}O_y$

3 $Na^+$ sites

**(b) Phase diagram upon charge of $Na//Na_3V_2(PO_4)_2F_3$**

Potential (*Volts vs. $Na^+$/Na*)

⊠ = 2-phase reaction

▨ = monophasic solid solution

**3** $Na_3VPF$; Amam

**2.4** $Na_{2.4}VPF$; (♦)

**2.2** $Na_{2.2}VPF$; I4/mmm

**2** $Na_2VPF$; "I4/mmm" (♦)

**1.3**-**1.8** $Na_xVPF$; I4/mmm

**1** NaVPF; Cmc2₁

♦ = superstructure

x (composition in $Na_xV_2(PO_4)_2F_3$)
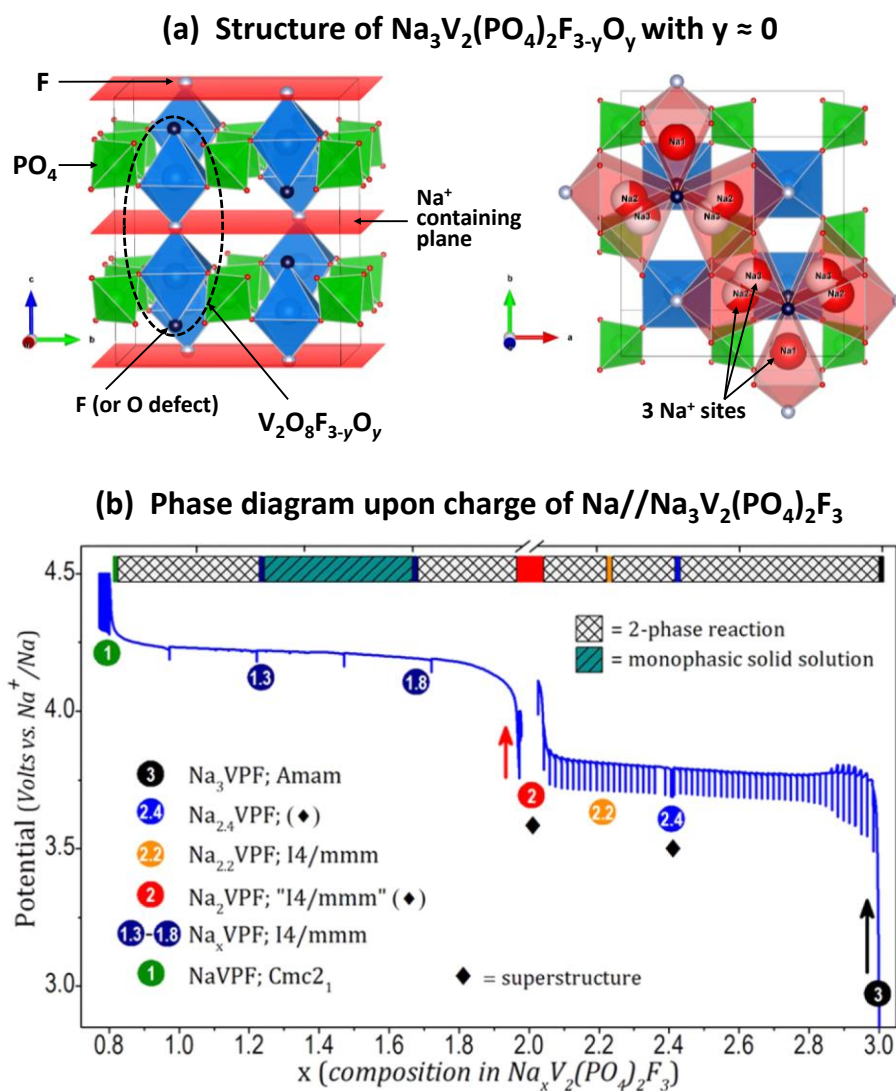
**Figure 2**: Comparison of the experimental SXRPD patterns recorded for the three NVPF samples. The indexation of the diffraction lines is given in the *Amam* space group. The inset emphasizes the subtle shift of the (006) reflection for the C-VPO$_4$ NVPF compound, and more generally of all the (00$l$) diffraction lines.
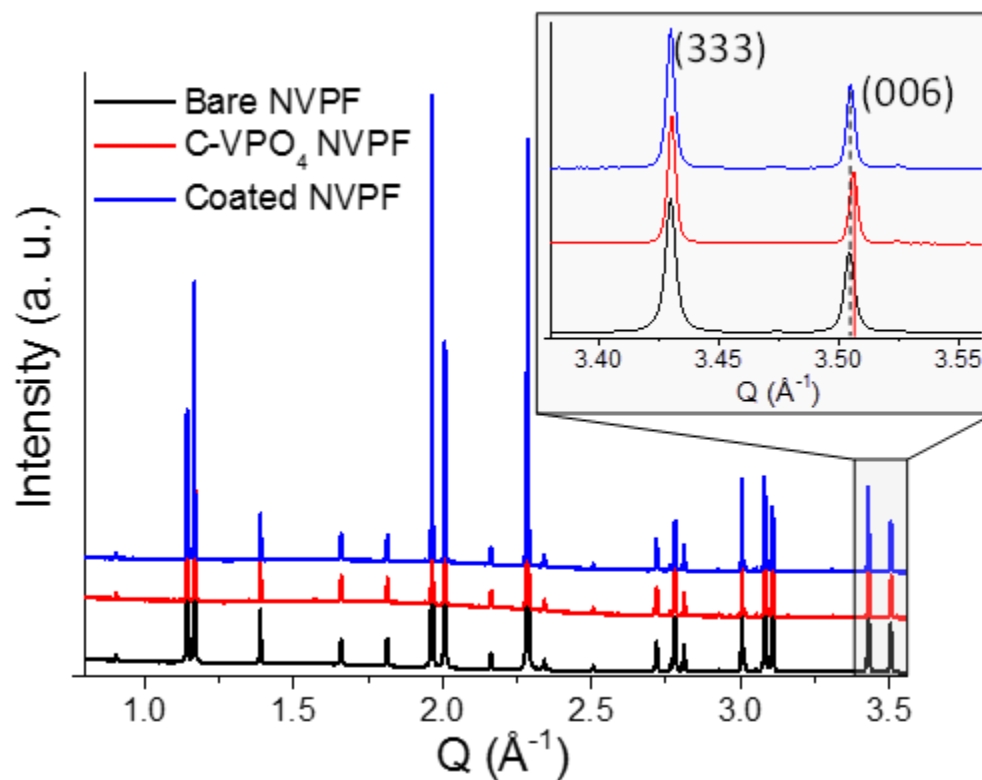
**Figure 3**: Comparison of the a) $^{23}Na$ and b) $^{31}P$ MAS NMR spectra of the three NVPF samples and of a slightly oxidized sample $Na_3VPF_{2.8}O_{0.2}$. The shift is given in ppm for each signal, as well as its environment in vanadium. As an example, the $^{31}P$ MAS NMR signal observed at 6100 ppm corresponds to the $P^{5+}$ ions with 4 $V^{3+}$ in their close vicinity.
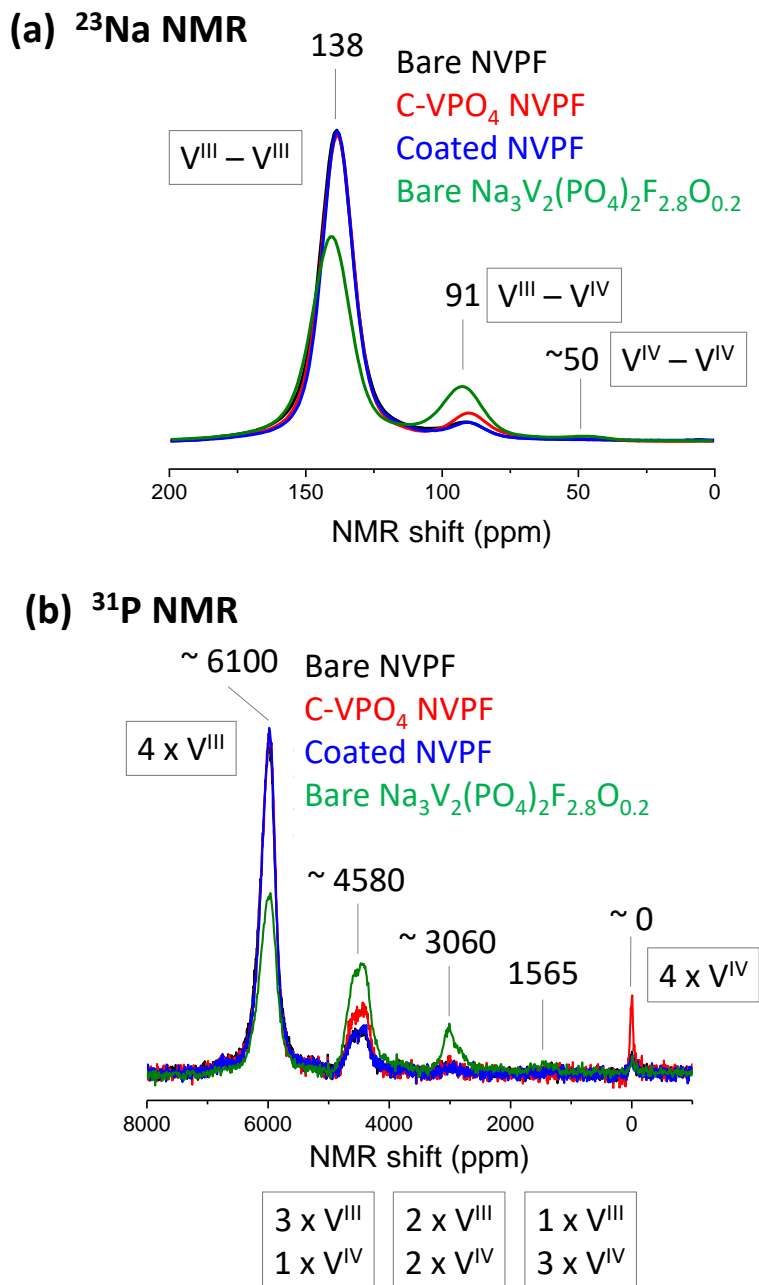
**Figure 4**: Scanning electron micrographs obtained for the three NVPF samples (bare NVPF, C-VPO$_4$ NVPF and coated NVPF).
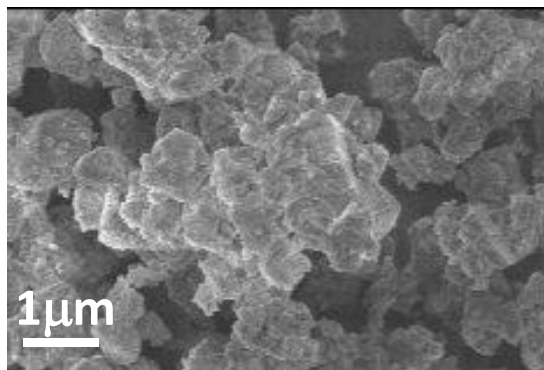
## Bare NVPF



## C-VPO$_4$ NVPF
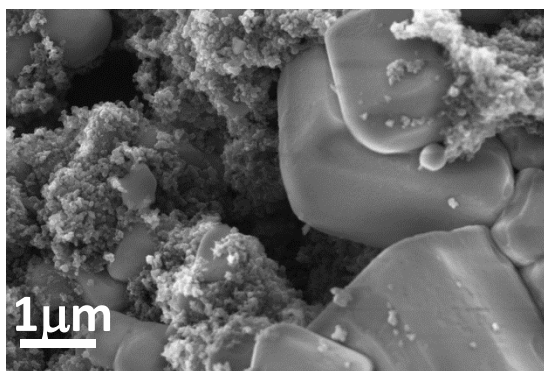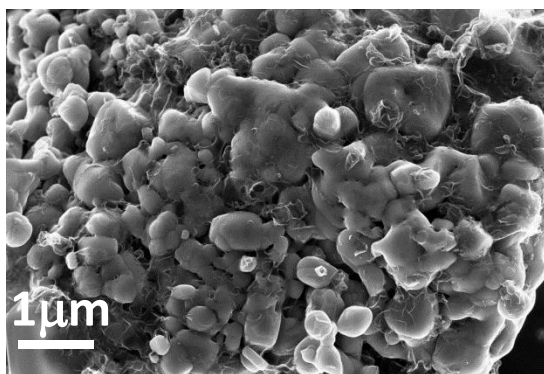


## Coated NVPF

**Figure 5**: Comparison of the SXRPD patterns recorded *operando* during $Na^+$ deintercalation from the three NVPF samples (Bare NVPF, C-VPO$_4$ NVPF and Coated NVPF), between the compositions Na$_3$VPF and Na$_1$VPF, at a C/2 cycling rate.

*(please on a full column)*

**Bare NVPF**
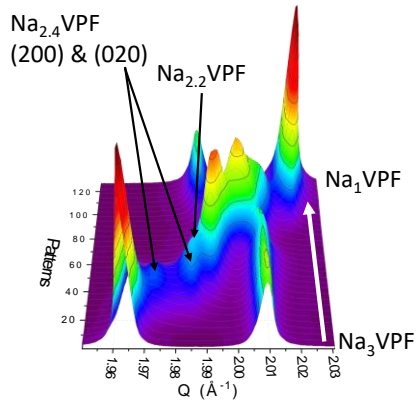


**C-VPO$_4$ NVPF**
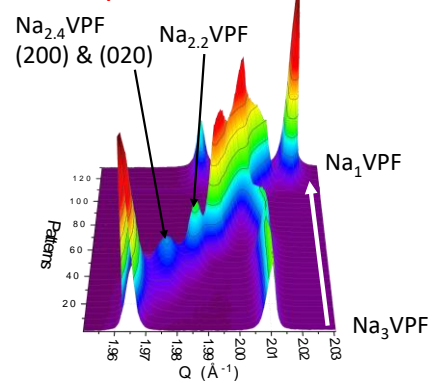


**Coated NVPF**
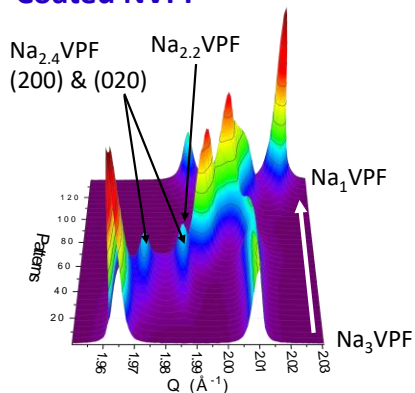
**Figure 6**: Comparison of the electrochemical curves obtained for the three NVPF samples studied within the *in situ* cell and cycled at C/2 up to 4.4 V vs. Na⁺/Na. A floating (i.e. potential maintained constant) was performed at 4.4 V at the end of the charge during approximately 10 minutes. The corresponding SXRPD patterns are given in **Figure 5**.
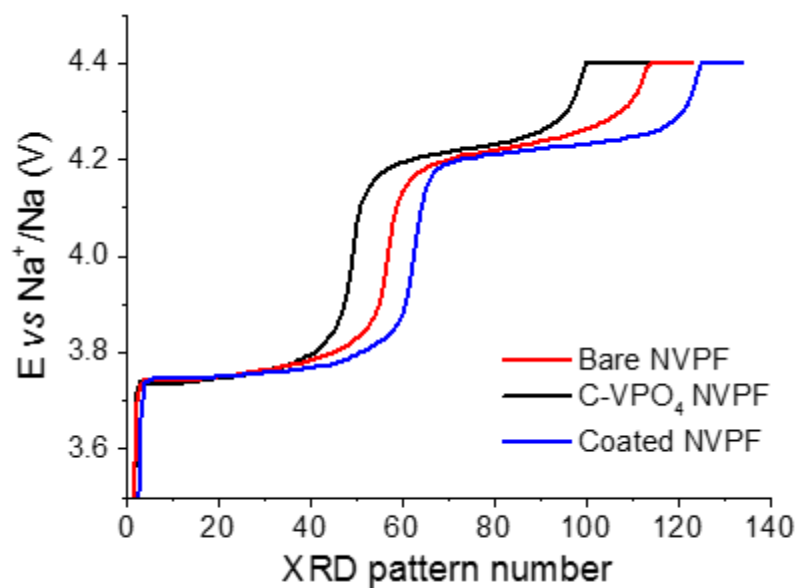
**Figure 7**: Comparison of the SXRPD patterns obtained *operando*, at the composition close to $Na_{2.4}$, for the three NVPF samples and for the partially oxidized sample Bare $NVPF_{2.8}O_{0.2}$.
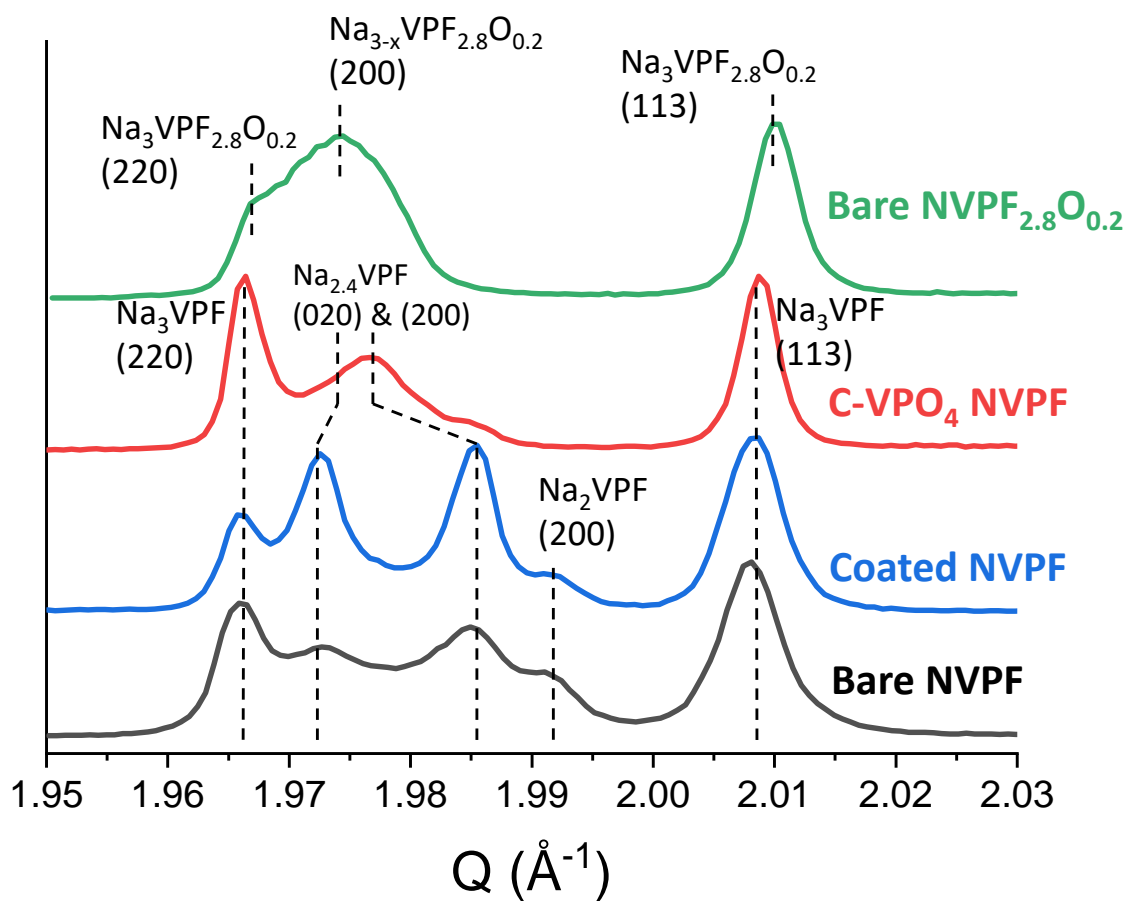
**Figure 8**: SXRPD patterns recorded *operando* during Na$^+$ de-intercalation from C-VPO$_4$ NVPF and Bare NVPF$_{2.8}$O$_{0.2}$ at a rate of C/2, between the compositions Na$_3$VPF (resp. Na$_3$VPF$_{2.8}$O$_{0.2}$) and Na$_2$VPF (resp. Na$_2$VPF$_{2.8}$O$_{0.2}$).
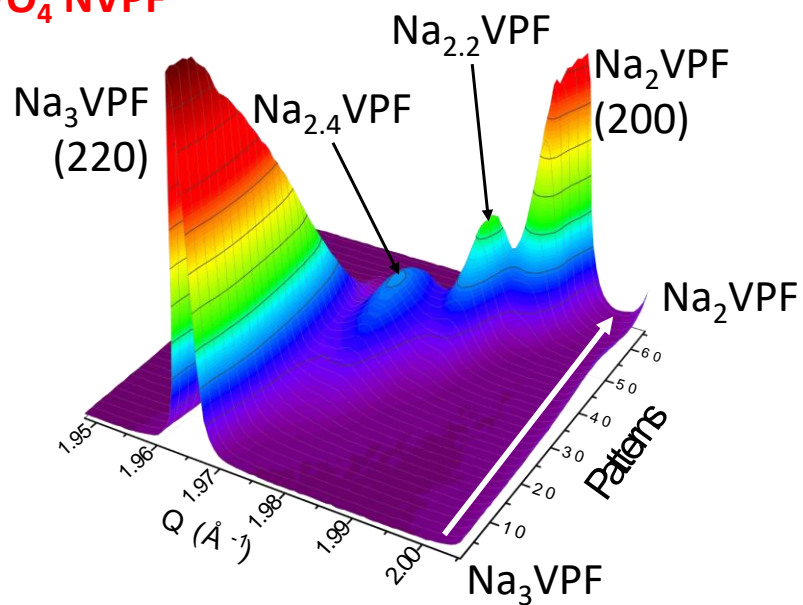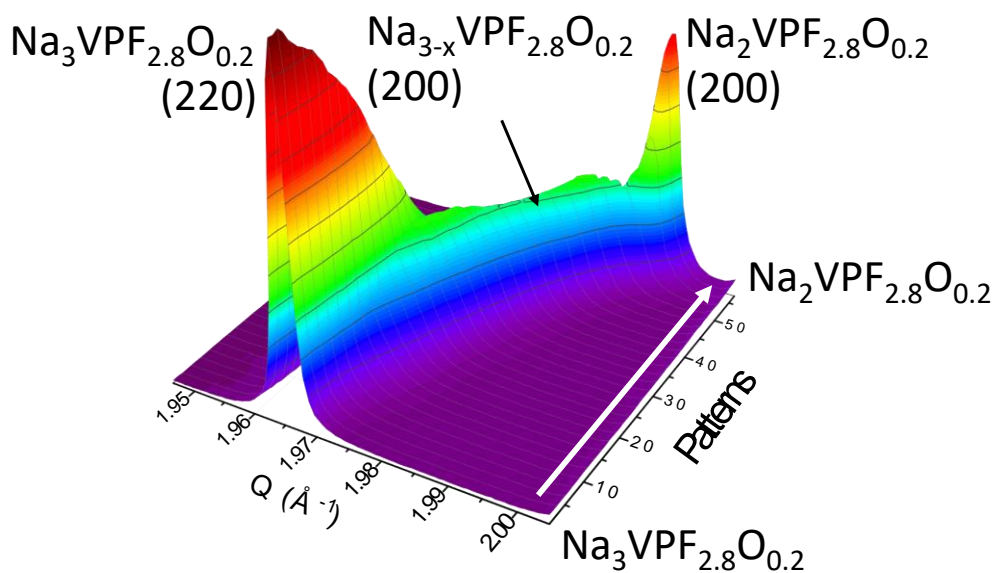
**Figure 9**: Voltage-composition curves obtained for coated NVPF in *in situ* electrochemical cells cycled in different conditions: C/10, 5C and 25C rates at room temperature (in blue, grey and yellow respectively), and C/10 rate at 0°C (in red).
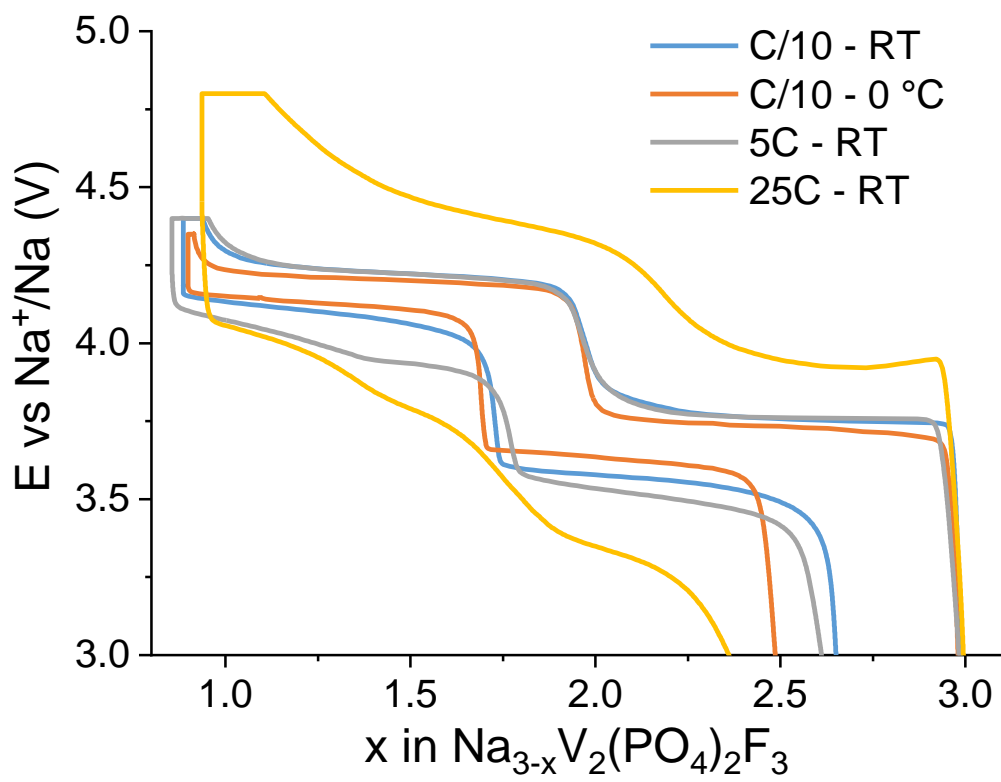
**Figure 10**: (a) 2D plot of a selected angular domain of the SXRPD patterns recorded *operando* during Na⁺ deintercalation from coated NVPF at C/10 rate and 0°C, between the compositions Na₃VPF and Na₁VPF. (b) Corresponding 3D plot between the compositions Na₃VPF and Na₂VPF.
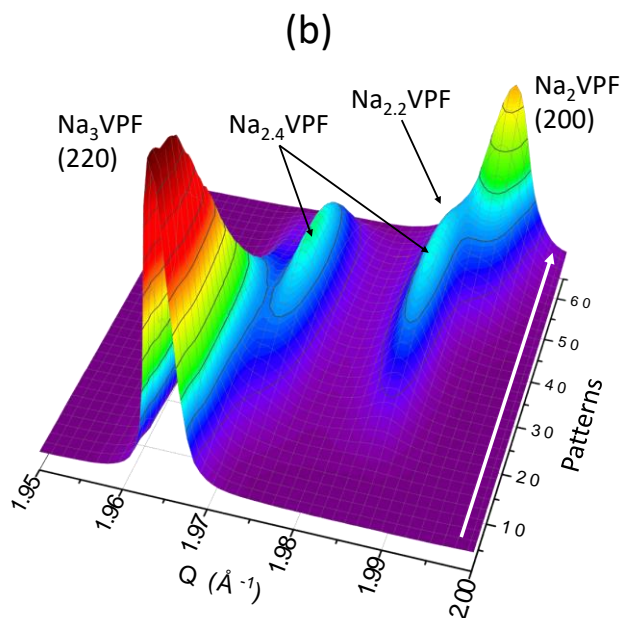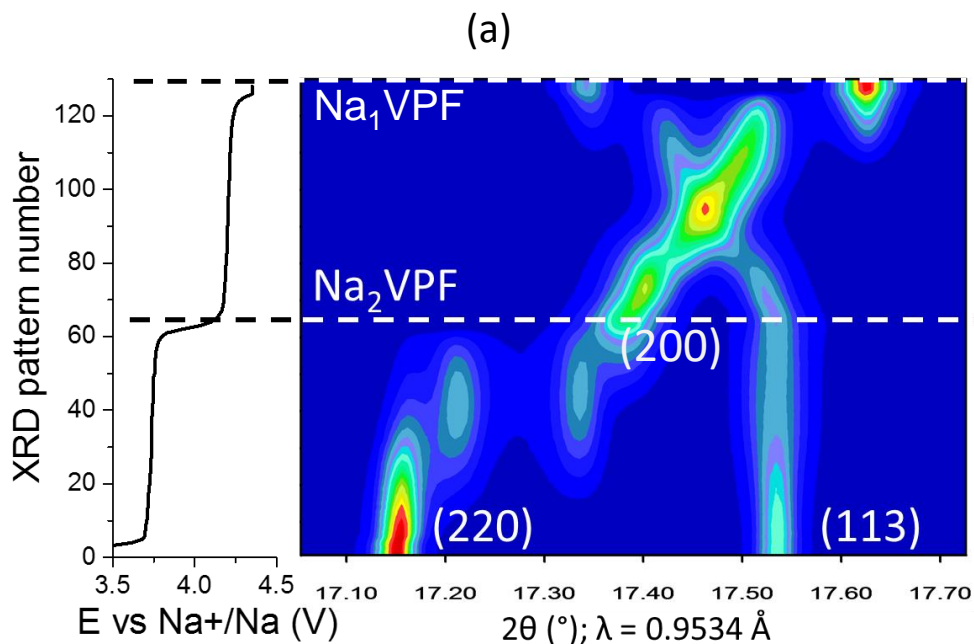


Coated NVPF, at C/10 and at 0°C

**Figure 11**: 2D plot of a selected angular domain of the SXRPD patterns recorded *operando* during Na$^+$ deintercalation at 5C (top) and 25C (bottom) from coated NVPF, between the compositions Na$_3$VPF and Na$_1$VPF.
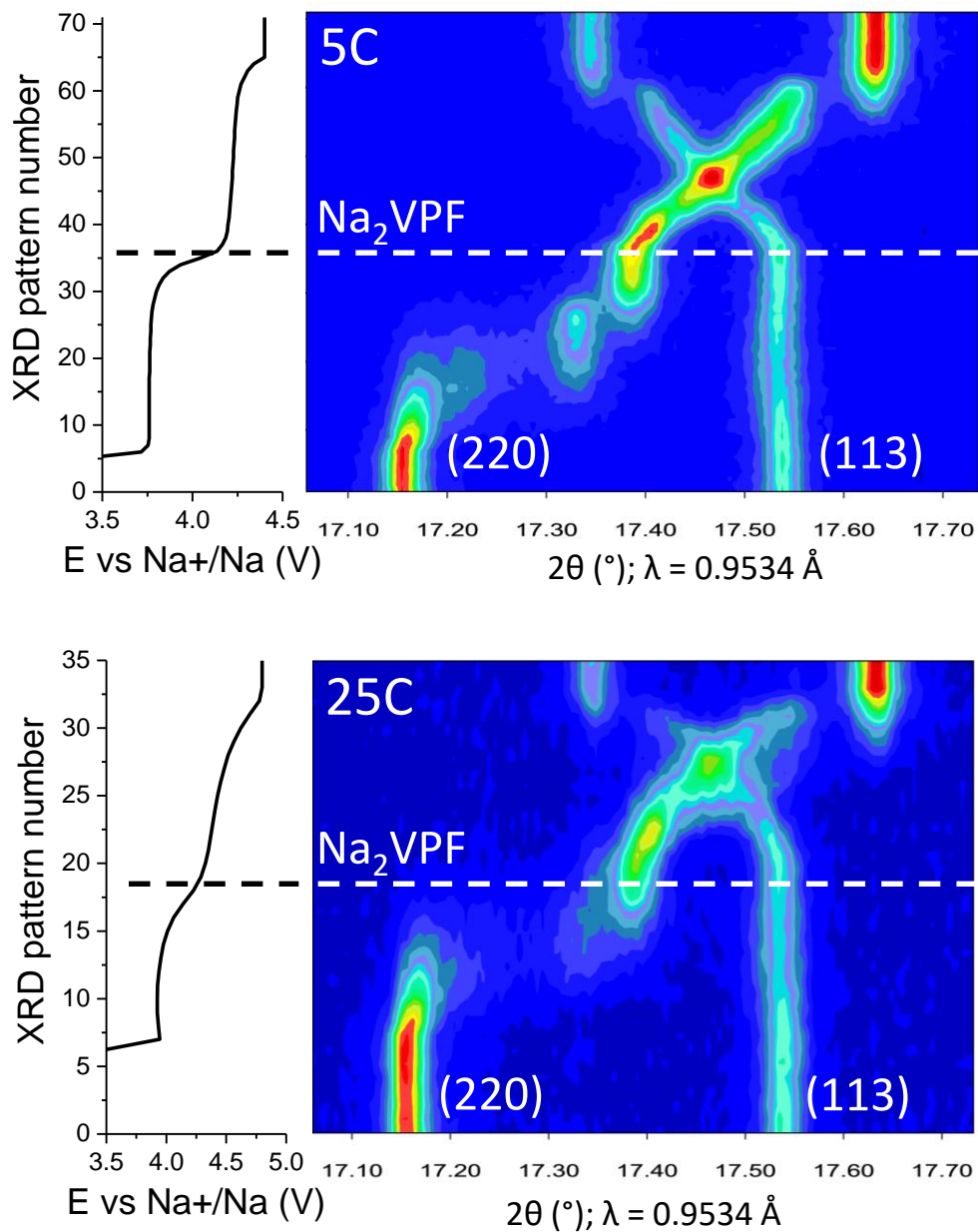
**Figure 12**: 2D plot of selected angular domain of the experimental *operando* SXRPD patterns recorded for coated NVPF, between the compositions $Na_3VPF$ and $Na_2VPF$, during the GITT experiment performed with 25C current pulses followed by 20 minutes relaxation.
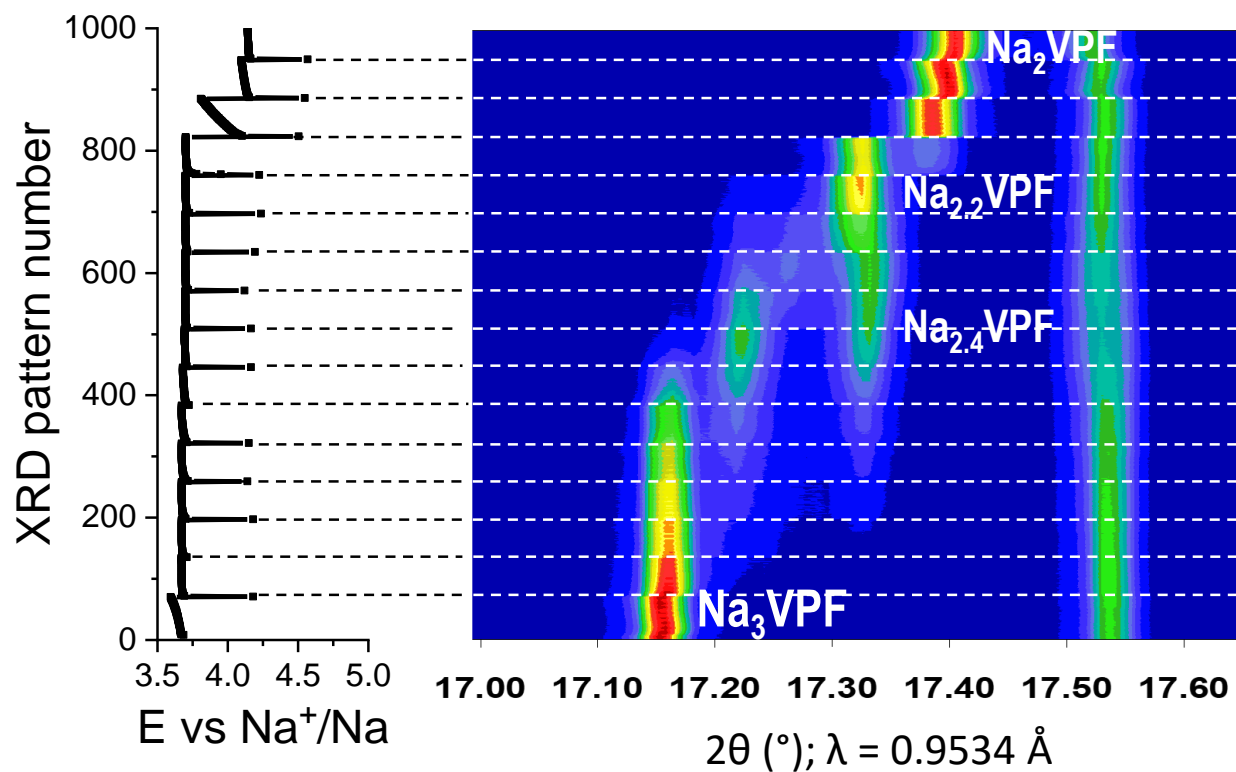
**Figure 13**: SXRPD patterns collected in microdiffraction conditions, at three positions of the electrode separated by 1mm and at different cycling rates (C, 10C and 20C).

*This figure has to be included as a two columns*
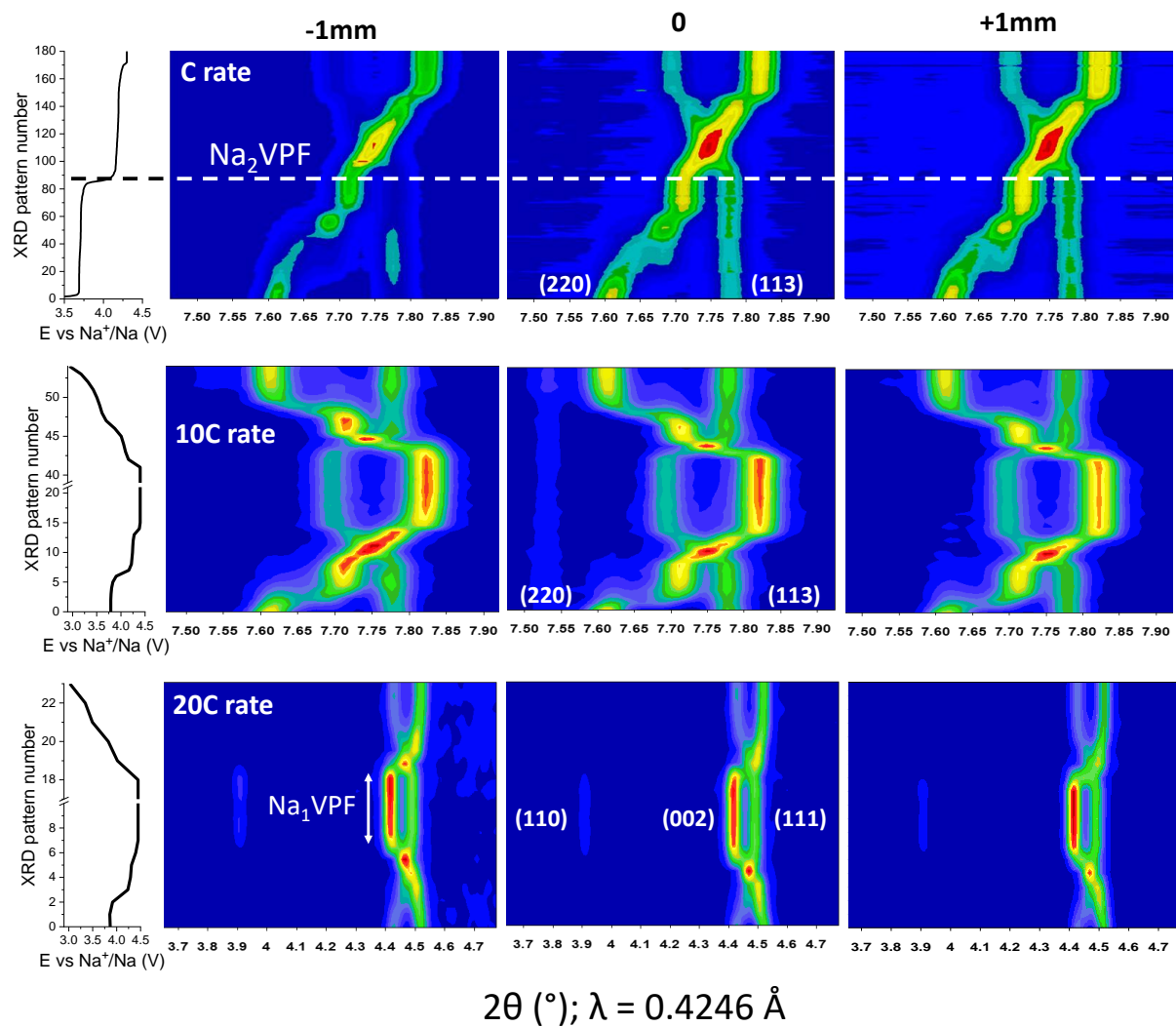


2θ (°); λ = 0.4246 Å

Figure 14: Performance obtained in 18650 cells: (a) long term cyclability at a 1C rate upon charge and discharge for a 75 Wh/kg prototypes and (b) rate capabilities for 55 Wh/kg prototypes.
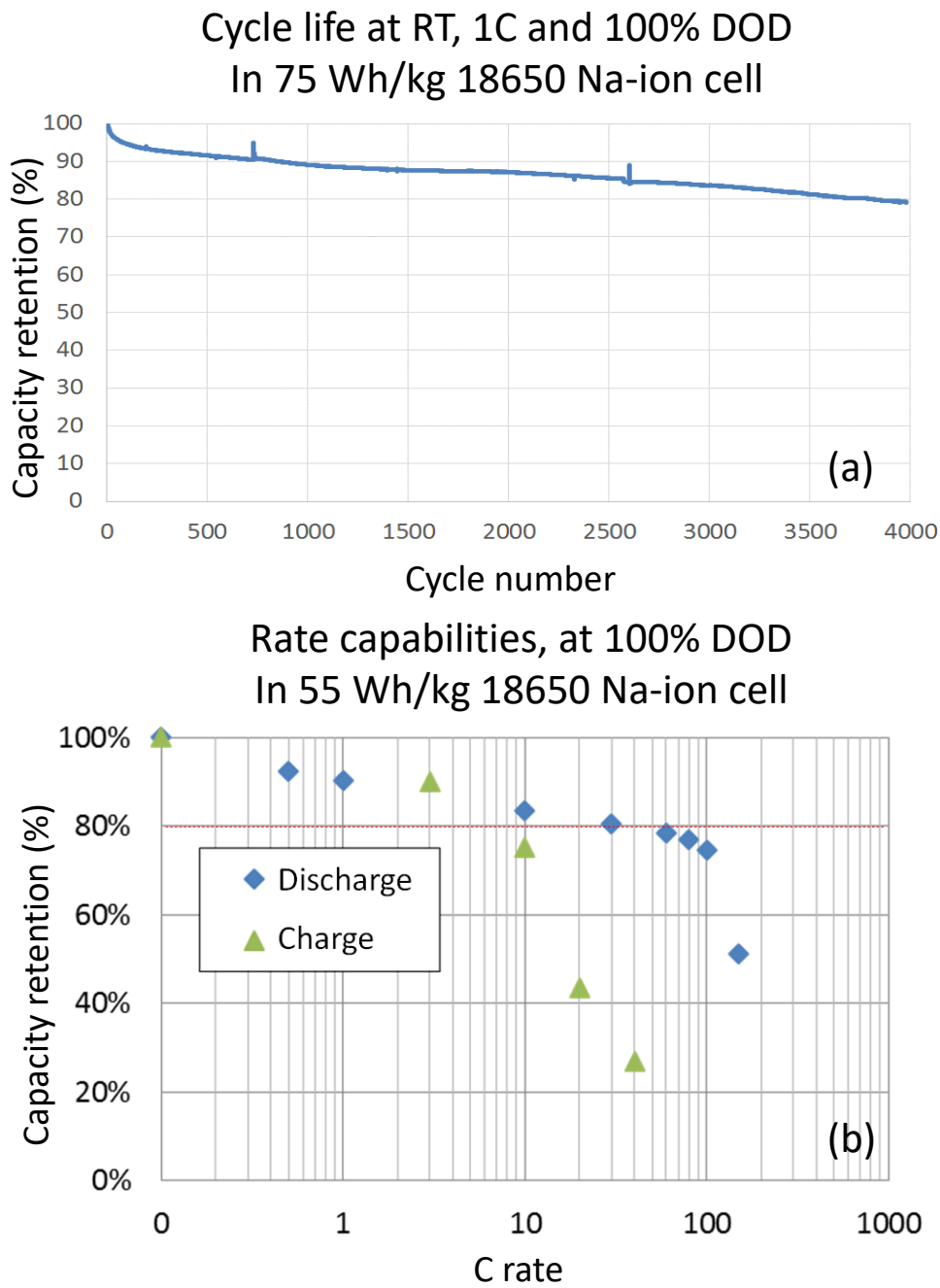


**Table captions**

**Table 1**: The cell parameters determined for the intermediate phases $Na_xVPO_4F$ (x = 2.4, 2 and 1) formed upon $Na^+$ deintercalation from the pristine phase $Na_3V_2(PO_4)_2F_3$ are compared for the three NVPF samples (bare NVPF, C-VPO$_4$ NVPF and coated NVPF).

| Compounds | Compositions | | | |
|---|---|---|---|---|
| | **Na$_3$VPF** | **Na$_{2.4}$VPF** | **Na$_2$VPF** | **Na$_1$VPF** |
| | Space group and Unit cell parameters (Å and Å$^3$) | Space group and Unit cell parameters (Å and Å$^3$) | Space group and Unit cell parameters (Å and Å$^3$) | Space group and Unit cell parameters (Å and Å$^3$) |
| **Bare NVPF** | ***Amam*** <br> a = 9.0307(1) <br> b = 9.0449(1) <br> b/a = 1.0016 <br> c = 10.7538(1) <br> V = 878.39(3) - V/Z = 219.60 | ***Immm*** (average) <br> a = 6.3230(1) <br> b = 6.3729(1) <br> b/a = 1.0079 <br> c = 10.7644(1) <br> V = 433.76(3) - V/Z = 216.88 | ***I4/mmm*** (average) <br> a = 6.3014(1) <br> b = 6.3014(1) <br> b/a = 1 <br> c = 10.7946(1) <br> V = 428.63(3) - V/Z = 214.31 | ***Cmc2$_1$*** <br> a = 8.7819(1) <br> b = 8.7962(1) <br> b/a = 1.0016 <br> c = 11.0045(1) <br> V = 850.07(3) - V/Z = 212.52 |
| **C-VPO$_4$ NVPF** | ***Amam*** <br> a = 9.0295(1) <br> b = 9.0446(1) <br> b/a = 1.0016 <br> c = 10.7481(1) <br> V = 877.78(3) - V/Z = 219.44 | ***Immm*** (average) <br> a = 6.3467(1) <br> b = 6.3603(1) <br> b/a = 1.0029 <br> c = 10.7718(1) <br> V = 434.82(3) - V/Z = 217.41 | ***I4/mmm*** (average) <br> a = 6.3038(1) <br> b = 6.3038(1) <br> b/a = 1 <br> c = 10.7982(1) <br> V = 429.10(3) - V/Z = 214.55 | ***Cmc2$_1$*** <br> a = 8.7867(1) <br> b = 8.8014(1) <br> b/a = 1.0017 <br> c = 11.0064(1) <br> V = 851.18(3) - V/Z = 212.80 |
| **Coated NVPF** | ***Amam*** <br> a = 9.0294(1) <br> b = 9.0448(1) <br> b/a = 1.0017 <br> c = 10.7515(1) <br> V = 878.06(3) - V/Z = 219.52 | ***Immm*** (average) <br> a = 6.3254(1) <br> b = 6.3655(1) <br> b/a = 1.0063 <br> c = 10.7766(1) <br> V = 433.91(3) - V/Z = 216.96 | ***I4/mmm*** (average) <br> a = 6.3057(1) <br> b = 6.3057(1) <br> b/a = 1 <br> c = 10.7976(1) <br> V = 429.33(3) - V/Z = 214.67 | ***Cmc2$_1$*** <br> a = 8.7864(1) <br> b = 8.8021(1) <br> b/a = 1.0018 <br> c = 11.0085(1) <br> V = 851.38(3) - V/Z = 212.84 |